Pergamon

0956-7151(94)00378-5

Acta metall. mater. Vol. 43, No. 4, pp. 1467–1476, 1995
Copyright © 1995 Elsevier Science Ltd
Printed in Great Britain. All rights reserved
0956-7151/95 $9.50 + 0.00

ON THE CORRELATION OF MICROSTRUCTURE AND ELECTROMAGNETIC PROPERTIES OF HEAVILY COLD WORKED Cu–20 wt% Nb WIRES

F. HERINGHAUS†, D. RAABE‡ and G. GOTTSTEIN

Institut für Metallkunde und Metallphysik, Kopernikusstrasse 14, Rheinisch-Westfälische Technische Hochschule Aachen, Germany

(Received 15 July 1994)

Abstract—Fibre or ribbon reinforced *in situ* metal matrix composites (MMCs) consisting of Cu and 20 wt% Nb were produced by large strain wire drawing. The microstructure of the composites was investigated by means of optical and electron microscopy. The normal and superconducting properties of the MMC wires in the presence of external magnetic fields were examined and compared to the electromagnetic properties of pure Cu wires. The findings are discussed on the basis of the microstructural changes during deformation. The current results substantiate that the amount of internal boundaries and the filament spacing have considerable influence on the normal and superconducting properties of Cu–20%Nb.

Zusammenfassung—Faserverstärkte *in situ* Verbundwerkstoffe mit metallischer Matrix (MMCs) aus Cu und 20 gew.% Nb wurden durch hohe Drahtverformung hergestellt. Die Mikrostruktur der Verbundwerkstoffproben wurde mit Hilfe licht- und elektronenoptischer Mikroskopie untersucht. Die normal- und supraleitenden Eigenschaften der MMC-Drähte wurden unter dem Einfluß äußerer magnetischer Felder gemessen und mit den elektromagnetischen Eigenschaften reiner Cu-Drähte verglichen. Die ermittelten Daten werden auf der Basis der mikrostrukturellen Entwicklung im Verlauf der Verformung diskutiert. Die vorliegenden Ergebnisse belegen, daß der Anteil an inneren Grenzflächen und der Faserabstand einen beträchtlichen Einfluß auf die normal- und supraleitenden Eigenschaften von Cu–20%Nb haben.

1. INTRODUCTION

Copper and Niobium have negligible mutual solubility in the solid state [1, 2]. Ribbon or fibre reinforced *in situ* processed metal matrix composites (MMCs) can hence be manufactured by large degrees of deformation, e.g. by wire drawing or rolling of a cast ingot.

Competitive binary systems of Cu with Ta, Cr, Mo or V show a similar thermodynamical behaviour, but exhibit considerable shortcomings as compared to Cu–Nb. The density of Ta, Cr, Mo and V strongly deviate from that of Cu so that gravitational segregation during solidification and the increase of the specific density of the final alloy deteriorate its potential for technological applications. Moreover, the melting temperatures of Ta and Mo are much higher than that of Nb which complicates the melting process.

Cu and Nb reveal almost equal densities ($\rho_{Cu} = 8890\ kg/m^3$, $\rho_{Nb} = 8580\ kg/m^3$). Therefore gravitational segregation does not occur, practically. Increased Nb content leads to a decrease of ductility, i.e. of elongation to fracture [3], and to a degradation of electrical conductivity [4]. Thus, an alloy containing 20 wt% Nb appears to combine optimum electrical and mechanical properties. Cu–Nb composites have been under intensive investigation for the past 15 yr mainly for the following two reasons.

(1) The tensile strength of the deformed material is very high, in particular much greater than expected from the rule of mixtures [5–7]. Several models have been proposed to explain the observed strength anomaly on the basis of microstructural mechanisms. The barrier model by Spitzig and coworkers [6] attributes the strength to the difficulty of propagating plastic flow through the f.c.c.–b.c.c. interfaces (f.c.c = face centred cubic, b.c.c. = body centred cubic). Funkenbusch and Courtney interpret the strength in terms of geometrically necessary dislocations owing to the incompatibility of plastic deformation of the b.c.c. and f.c.c. phase [7]. In fact, both models succeed in describing the observed increase of strength assuming reasonable fitting parameters. In a recent approach, Raabe and Hangen [8] have suggested a physical model which accounts for the observed dislocation structures and for the crystallographic textures of both phases. In such an approach the high tensile strength can be described nearly without using fitting parameters.

†Present address: National High Magnetic Field Laboratory, Tallahassee, Florida, U.S.A.
‡To whom all correspondence should be addressed.

(2) Owing to the observed combination of high strength and good electrical conductivity Cu–Nb based MMCs are considered as candidate materials for the production of highly mechanically stressed electrical devices such as application in long-pulse high-field resistive magnets [9–11]. The potential use of these compounds, however, is much more widespread, e.g. applications in electronic devices in automobiles or as conducting frames in microelectronics are conceivable.

Whereas the microstructure of Cu–20%Nb and its electrical properties have been the subject of thorough studies in the past, a rigorous correlation of microstructure and electromagnetic behaviour has not yet been obtained. The current work is primarily concerned with the investigation of the normal and superconducting properties of Cu–20%Nb compounds and the correlation of these properties to microstructure.

2. EXPERIMENTAL

The Cu and the Cu–20 wt%Nb alloys were melted in an induction furnace using a frequency of 10 kHz and a power of 30 kW [12]. The Cu and the Nb both had an initial purity of at least 99.99 wt%. Ingots of 18 mm diameter were cast under an Argon atmosphere at a pressure of 0.8×10^5 Pa. According to the Cu–Nb phase diagram [1] a melting temperature of at least 1750°C is recommended for Cu 20%Nb. Other authors [2], however, reported the occurrence of a miscibility gap in the liquid phase due to the presence of interstitial foreign atoms, especially of H, N, C and O. Hence a temperature of at least 1830–1850°C was employed in order to assure complete dissolution of the Nb. A crucible and a mould of high purity graphite were used. The mould was preheated to about 600°C to ensure good fluidity and filling.

From the cylindrical ingots wires were produced by rotary swaging and subsequent drawing through hard metal drawing bench dies without intermediate annealing. The final diameter was 0.12 mm corresponding to a true strain of $\eta = 10$ ($\epsilon = 99.995\%$).

For investigation of the microstructure, scanning electron microscopy (SEM) and optical microscopy were employed. The resistivity measurements were carried out by means of the d.c. four-probe technique with currents between 10 and 100 mA. To study the normal and superconducting properties under externally imposed magnetic fields up to 15 T within the temperature range 3–300 K, an Oxford Instruments superconducting magnet was used. This magnet possesses a high field homogeneity and stability. A set of two samples, i.e. a Cu and a Cu–20%Nb wire having the same degree of deformation, were positioned in the centre of the superconducting magnet in such a way that the direction of the external magnetic force was perpendicular to the current flow in the wires. The data were taken continuously during cooling. The cooling rate was controlled using a small heater, attached close to the samples, and by addition of a He exchange gas. For the measurement of the temperature a carbon-glass resistance sensor was applied. The values of the voltage drop were averaged from measurements with opposite polarity. The polarity was changed with a frequency of about 1 Hz. Within the temperature range 300–3 K, about 2000–3000 data points were taken. In the corresponding diagrams merely a small fraction of the total data is represented owing to the use of discrete symbols. Errors due to thermal expansion and thermal inequilibrium were neglected. The total error was estimated to be less than 3%.

3. RESULTS

Microstructure

Figure 1(a) shows the microstructure of the as-cast Cu–20%Nb alloy. The primary Nb dendrites (light) are embedded in the Cu matrix (dark). After selectively dissolving the Cu matrix by use of HNO_3, quantitative metallography was carried out on the isolated dendrites [Fig. 1(b) and (c)]. This technique allows to precisely account for the three-dimensional morphology of the Nb dendrites. The densely covered primary dendrites were seen to branch out up to the third generation [Fig. 1(c)]. Whereas the orientations of the primary Nb dendrites were randomly distributed in the as-cast samples [13, 14] the dendritic arms were commonly aligned parallel to the crystallographic ⟨100⟩ directions [15]. In the as-cast state the mean diameter of the secondary dendrites, which are considered to have a large influence on the properties during processing, was $d_0 = 2.2 \pm 0.4\ \mu$m. The dendrite diameter increased from the surface to the centre of the wire.

The evolution of the morphology of the Nb dendrites into elongated fibres is shown in the micrographs in Fig. 2(a–c). After small amounts of deformation ($\eta = 2.2$, $\epsilon = 89\%$) the Nb morphology appeared quite inhomogeneous [Fig. 2(a)]. Whereas some dendrite arms revealed considerable elongation, others appeared almost undeformed [Fig. 2(a)]. After higher amounts of deformation ($\eta = 4.6$, $\epsilon = 99\%$) the filaments had a more uniform shape [Fig. 2(b)]. After the highest deformation ($\eta = 10$, $\epsilon = 99.995\%$) an average fibre diameter of about 130 nm and a filament thickness of 60 nm was found. The smallest filaments, however, revealed a thickness below 50 nm at this stage of deformation [Fig. 2(c)]. Some fibres consisted of a thick part with elongated thin tails, as marked by the arrow in [Fig. 2(c)].

In the heavily deformed *in situ* MMC all filaments were aligned parallel to the wire axis [13, 16, 17]. The random orientation distribution of the dendrite axes as shown in the micrographs of Fig. 2, is an artifact from the SEM sample preparation.

The evolution of the deformation of the Nb filaments, as calculated from the metallographic data, is given as a function of the wire deformation in

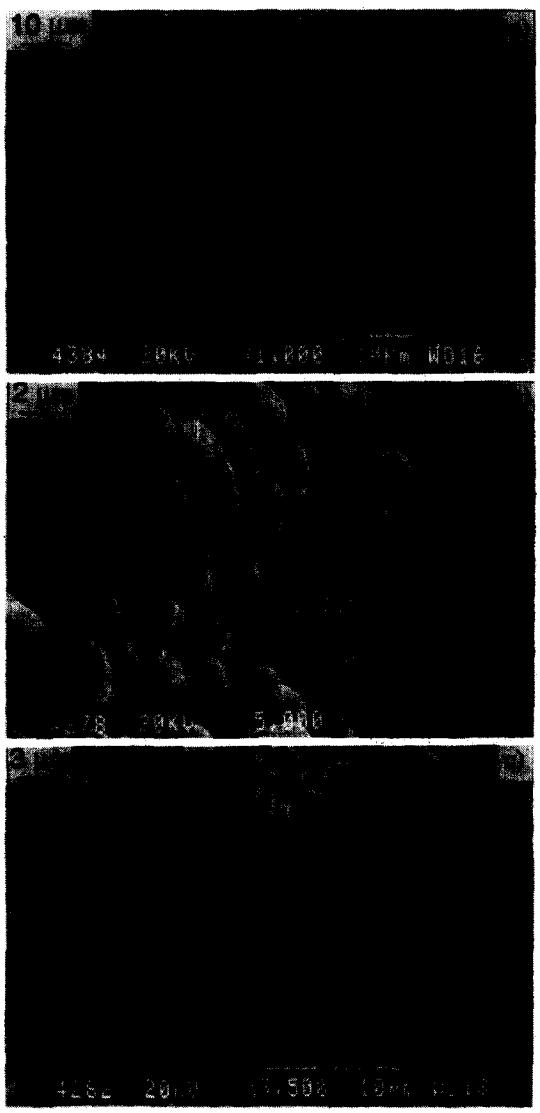

Fig. 1. SEM micrographs of as-cast Cu–20 wt%Nb. (a) Cross-section, primary Nb dendrites in Cu matrix; (b) isolated Nb dendrites, Cu matrix dissolved; (c) isolated Nb dendrites, Cu matrix dissolved. Dendrites up to third generation can be recognized.

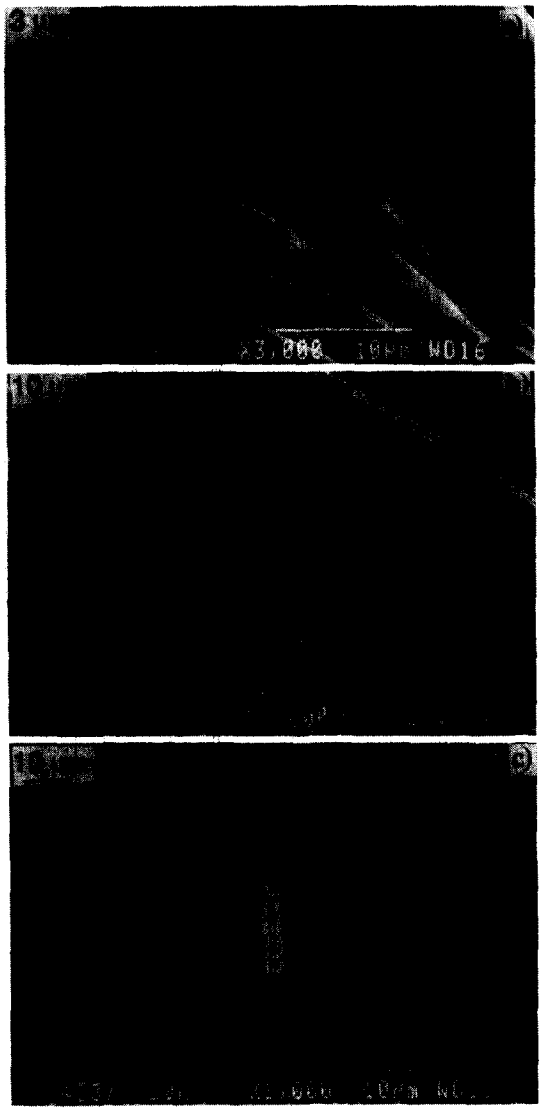

Fig. 2. SEM micrographs of Nb filaments, isolated by dissolving the Cu matrix at different degrees of wire deformation. (a) $\eta = 2.2$ ($\epsilon = 89\%$); (b) $\eta = 4.6$ ($\epsilon = 99\%$); (c) $\eta = 10$ ($\epsilon = 99.995\%$).

Fig. 3. The curve basically shows a linear dependence, although not a one to one correspondence. According to Fig. 3, a wire deformation of $\eta = 10$ ($\epsilon = 99.995\%$) corresponds to a Nb filament deformation of $\eta = 5.75$ (99.68%). The actual deformation of the Nb phase was thus generally lower than expected for a homogeneous deformation of the wire. If not explicitly stated otherwise, hereafter, η will be used to indicate wire deformation.

SEM micrographs taken from transverse sections after a deformation of $\eta = 7.6$ ($\epsilon = 99.95\%$) are given in Fig. 4(a, b). In Fig. 4(a) the curled and folded Nb phase can be observed. Also, the non-uniform morphology of the Nb fibres becomes apparent. At this strain the filament diameter range from 80 to 250 nm and the filament spacings from 150 to 1000 nm [Fig. 4(b)].

The wire hardness (200 g Vickers) is depicted as a function of deformation in Fig. 5. In the as-cast condition a value of about HV80 was measured. The hardness attained a plateau value of HV150 within the range $2 \leqslant \eta \leqslant 6$. At large deformation ($\eta > 6$) a strong increase of the hardness was observed, extending to a maximum value of HV325 at $\eta = 10$. For a deformation exceeding $\eta = 5$ the indentation cup showed a systematic distortion, i.e. the impression in radial direction was always larger than the diameter parallel to the wire axis, i.e. the hardness parallel to the radial direction of the wire was lower than parallel to the wire axis.

Electromagnetic properties

Measurements of the electrical resistivity were conducted at 295, 198 and 77 K. Figure 6 shows the dependences of the resistivity of both pure Cu (open

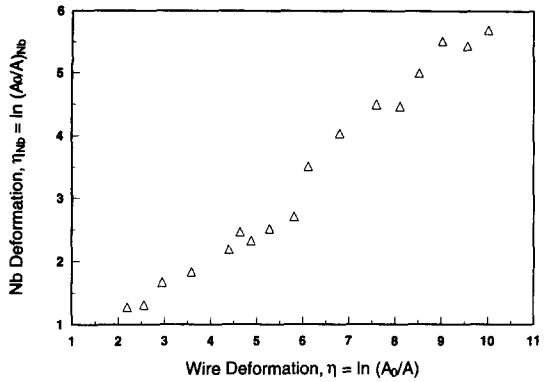

Fig. 3. Deformation of the Nb filaments as a function of the wire deformation.

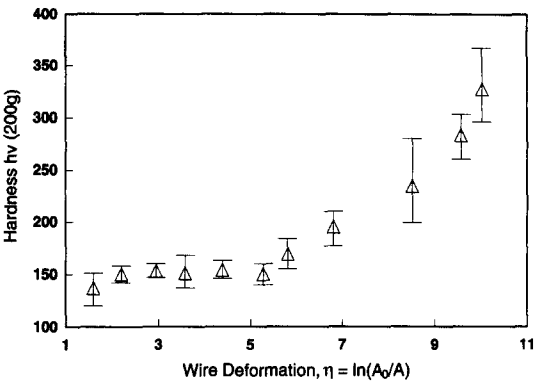

Fig. 5. Change of microhardness (Vickers, 200 g) of Cu–20 wt%Nb with increasing wire deformation.

symbols) and of Cu–20%Nb (solid symbols) at these temperatures on the wire deformation. The resistivity of pure Cu appears to be independent of the degree of deformation. The resistivity of Cu–20%Nb was always larger than for pure Cu and increased for $\eta > 6$. The measurements were repeated after a heat treatment of 5 h at 550°C. Within the resolution of the technique used, the resistivity of pure Cu was not affected by such annealing, but the resistivity of Cu–20%Nb noticeably decreased (Fig. 7). This drop of the resistivity was uniform up to about $\eta = 6$ ($\Delta\rho \approx 2\,\mu\Omega$mm) and became more pronounced with increasing deformation.

The effect of deformation on magnetoresistivity is given in Figs 8 and 9. Figure 8 shows the change of the specific magnetoresistance of maximum deformed Cu and Cu–20%Nb samples ($\eta = 10$) as a function of temperature for different externally imposed magnetic fields. Without external magnetic field the residual resistivity amounted to $\rho_{Cu(4.2\,K)} = 0.4\,\mu\Omega$mm for pure Cu and $\rho_{Cu\text{-}Nb(4.2\,K)} = 9\,\mu\Omega$mm for Cu–20%Nb. The residual resistivity ratio for pure Cu was $\rho_{295\,K}/\rho_{4.2\,K} = 48$ which is lower than expected from the initial purity of 99.99 wt%. It is hence assumed that during melting and casting the impurity content was augmented. The resistivity of pure Cu did not change significantly up to weak transverse magnetic fields of 2 T, but at higher fields a considerable increase was observed [Fig. 8(a)]. This effect became especially apparent at low temperatures. An external field of 15 T increased the residual resistivity of pure Cu at 4.2 K by $\Delta\rho = 0.7\,\mu\Omega$mm.

A similar behaviour was found for Cu–20%Nb [Fig. 8(b)]. Up to 4 T no significant contribution of the magnetic field on resistivity was observed. At a magnetic field force of 15 T, however, the resistivity was raised by $\Delta\rho = 0.5\,\mu\Omega$mm.

Without an external magnetic field the transition from the normal into the superconducting state is found for Cu–20%Nb at about 8 K [Fig. 8(b)]. With increasing magnetic field the corresponding transition temperature was observed to decrease. In Table 1 the onset (T_{onset}) and offset (T_{offset}) temperatures for the

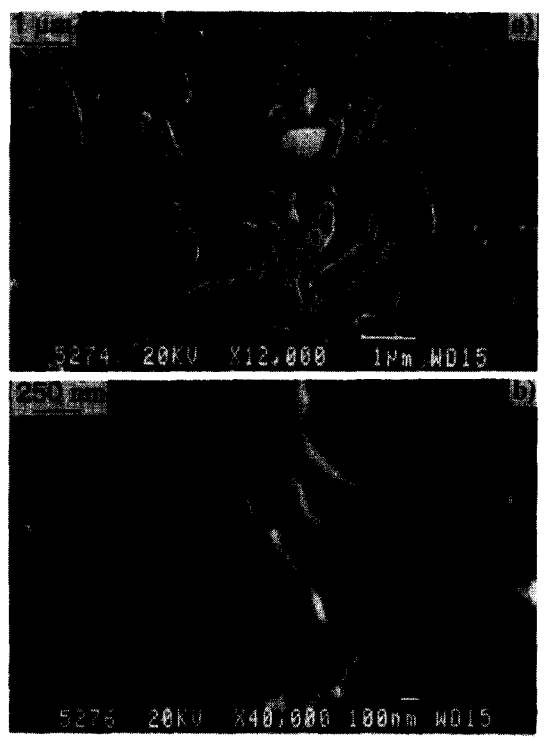

Fig. 4. (a) and (b). Cross-section of a Cu–20 wt%Nb wire, $\eta = 7.6$ ($\epsilon = 99.95\%$), at two different magnifications.

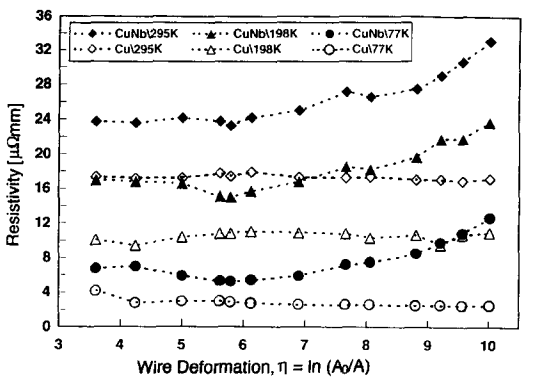

Fig. 6. Specific resistivity of Cu and Cu–20%Nb with progressing wire deformation for three different temperatures.

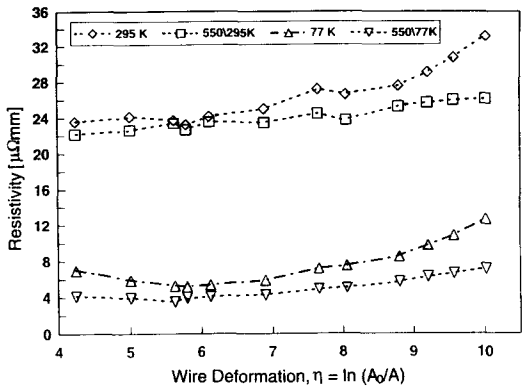

Fig. 7. Specific resistivity of Cu–20%Nb with progressing wire deformation measured at two different temperatures, with and without heat treatment at 550°C for 5 h.

superconductive transition are given. In Fig. 9, for a better distinction of the magnetoresistivity in Cu and Cu–20%Nb the ratio of the resistivities $\rho_B/\rho_{B=0}$ for an increasing magnetic field is plotted. Since Cu–20%Nb revealed superconducting properties at $B = 0$, 0.5, 1 and 2 T (onset only) the data were extrapolated. Both, Cu and Cu–20%Nb exhibited a linear dependence of $\rho_B/\rho_{B=0}$ on the magnetic field. But, pure Cu, which has a much lower residual resistivity and a higher magnetoresistance, revealed a higher slope than Cu–20%Nb.

The resistivity of Cu–20%Nb depended on the degree of deformation, i.e. on the microstructure as

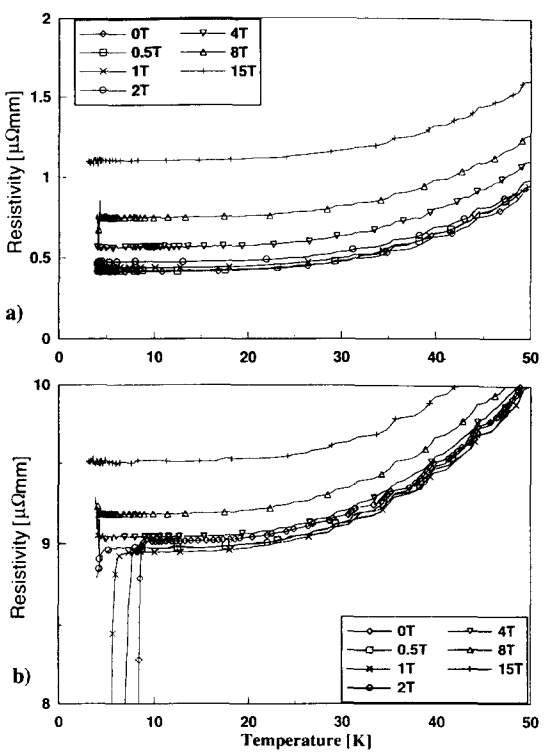

Fig. 8. Temperature dependent resistivity of Cu and Cu–20 wt%Nb for different externally imposed transverse magnetic fields ($\eta = 10$). (a) Cu; (b) Cu–20 wt%Nb.

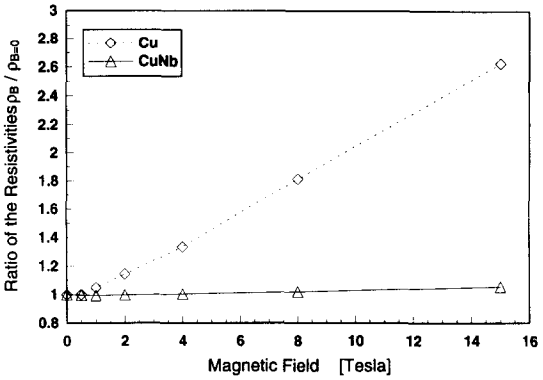

Fig. 9. Normalized resistivity $\rho(B)/\rho(B = 0)$ of Cu and Cu–20 wt%Nb ($\eta = 10$) exposed to a magnetic field B.

evident from Fig. 10. The samples showed a transition to the superconducting state at the same onset temperature. Both with and without applied external magnetic field the resistivity in the normal conducting state was higher for the sample which had undergone a larger thickness reduction.

An external transverse magnetic field led to a decrease of the critical temperature for both levels of deformation and to a shift of the curves relative to each other [Fig. 10(b)]. The onset temperature at $B = 1$ T for the more strongly deformed wire ($d = 0.12$ m, $\eta = 10$) was approx. 6 K, and for the less deformed wire ($d = 0.6$ mm, $\eta = 6.8$) about 5.3 K. Another difference in the transition to the superconducting state at $B = 1$ T as opposed to $B = 0$ T was the larger gap between T_{onset} and T_{offset} ($\Delta T \approx 1$ K for $B = 0$ T, $\Delta T \approx 1.7$ K for $B = 1$ T, e.g. for $d = 0.12$ mm).

A sweep of the magnetic field at 4.3 K also revealed a difference in the transition to the resistive state for both levels of deformation. The sample with $\eta = 6.8$ required a critical field of about $B = 1.3$ T, while the sample with $\eta = 10$ needed almost $B = 2$ T (Fig. 11). The critical temperature and the critical magnetic field force, which limit the range of the superconducting state, are given in Fig. 12.

4. DISCUSSION

Microstructure

Cu and Nb have a negligible mutual solubility in the solid state. In the as-cast condition the Nb phase reveals a dendritic morphology (Fig. 1). The average diameter of the secondary dendrites is about 2 μm. Compared to other production methods this value is quite small [6, 18] and thus ensures a high tensile strength after heavy deformation [6]. The observed inhomogeneity of the size of the Nb dendrites,

Table 1. Critical temperatures of Cu–20 wt% Nb at different magnetic fields, $\eta = 10$

B [T]	0	0.5	1	2
T_{onset}	8.5	7.8	6	4.5
T_{offset}	7.5	5.5	4.1	—

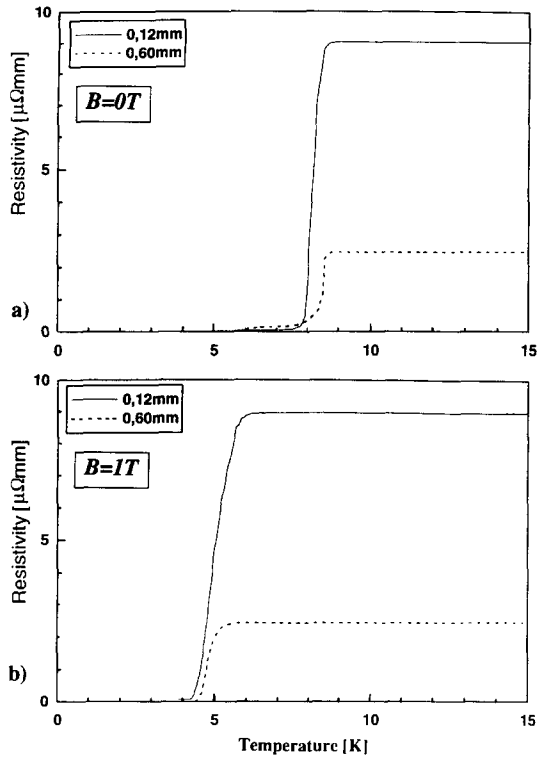

Fig. 10. Resistivity of Cu–20 wt%Nb as a function of the temperature for two different degrees of deformation ($d = 0.6$ mm [$\eta = 6.8$]; $d = 0.12$ mm [$\eta = 10$]). (a) $B = 0$ T, (b) B = 1 T.

characterized by the increase of the mean dendrite diameter from the surface to the centre of the wire cross-section can be understood in terms of the corresponding gradient of the cooling rate during casting of the initial sample. The high cooling rate at the sample surface did not only lead to a small dendrite diameter but also to a higher density of dendrites of second and third generation.

The observed inhomogeneous Nb morphology up to a deformation degree of $\eta \approx 2$ [Fig. 2(a)], showed that very heavy deformation is necessary to produce a homogeneous size distribution of the Nb filaments

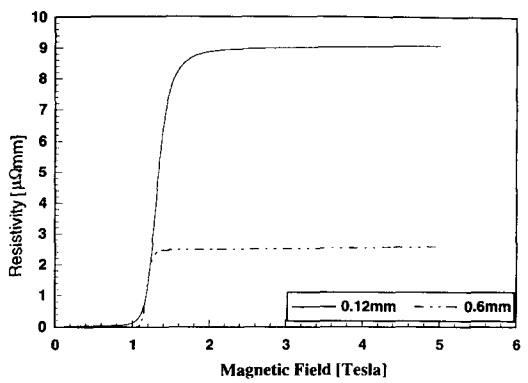

Fig. 11. Resistivity of Cu–20 wt%Nb with increasing magnetic field strength for two different degrees of deformation ($d = 0.6$ mm [$\eta = 6.8$]; $d = 0.12$ mm [$\eta = 10$]), $T = 4.3$ K.

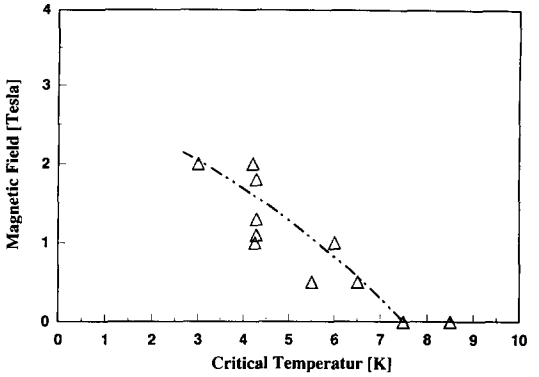

Fig. 12. Magnetic field of a Cu–20 wt%Nb superconductor as a function of the critical temperature ($\eta = 10$). This can be interpreted as a phasediagram of the superconducting state.

within the MMC [Fig. 2(b, c)]. This is due to several reasons. First, the strain distribution during wire drawing is inhomogeneous across the wire diameter, which results in an inhomogeneous dendrite morphology. Second, as indicated by the lower deformation of the Nb dendrites as compared to the Cu matrix (Fig. 3) and confirmed by the observed hardness plateau (Fig. 5) for $\eta < 6$, small degrees of deformation cause the initially randomly oriented dendrites [13, 16] to rotate towards an orientation parallel to the wire axis. After this alignment ($\eta \approx 6$) a massive cross-sectional area reduction of the dendrites was observed. Also it elucidates the finding that with regard to strength considerable deviations from the predictions of the linear rule of mixtures (ROM) were observed for high ($\eta > 6$) but not for low degrees of deformation. This is apparently the reason that for $\eta \approx 2$ [Fig. 2(a)] a mixture of highly deformed dendrites and almost undeformed ones were found next to each other. Moreover, the deformation is strongly influenced by the incompatibility of the deformation of the f.c.c. Cu and the b.c.c. Nb. Since the distribution of the Nb phase is inhomogeneous, the more ductile Cu phase has to undergo a higher deformation locally. This again modifies the local stress distribution within the wire, i.e. neither the actual Cu deformation nor the actual Nb deformation equals the true wire deformation.

After heavy deformation of the MMC all the Nb filaments are aligned parallel to the wire axis. As noted before, the random orientation of the fibres in Fig. 2 is an artifact introduced during specimen preparation. The strong bending of the filaments occurring subsequent to dissolving the Cu matrix (Fig. 2) indicates strong residual stresses, i.e. a high content of geometrically necessary dislocations.

Another striking feature of the Nb filaments is their flat and curled morphology when observed in the cross section of the wire (Fig. 4). While the wire deformation imposes a strain state with rotation symmetry about the drawing direction, the resulting shape of the Nb filaments does not reveal this

symmetry. This has to be attributed to the microscopic strain distribution and can be explained by the texture evolution of the Nb. As evident from X-ray and electron diffraction experiments as well as by Taylor type simulations, the b.c.c. Nb phase develops a ⟨110⟩ fibre texture during wire deformation ($\eta > 4$) [13, 16]. According to Hosford [19], this Nb texture allows for only two of the four ⟨111⟩ b.c.c. slip directions to contribute to plastic deformation parallel to the wire axis. However, the activation of only symmetrical slip systems causes a local plane strain deformation which leads, under the externally imposed axisymmetric flow, to a bent shape of the Nb phase, which is referred to as curling. This phenomenon only occurs in composites which consist of a b.c.c. and a f.c.c. phase. In f.c.c metals, where usually a ⟨111⟩ texture is generated during wire drawing, no planar slip is enforced, i.e. accordingly no curling is observed in composites comprising two f.c.c. phases.

The most significant consequence of the Nb curling is the strong increase of the total Cu–Nb phase boundary area. If the thickness of the phase boundary is assumed to be about 0.5 nm, the volume fraction of internal phase boundaries becomes comparable to the volume fraction of the second phase for $\eta > 6$ [20]. These data explain the importance of the phase boundaries for the composite properties and in particular for the electromagnetic behaviour.

Electromagnetic properties

The electrical resistivity of a metal arises from the scattering of conduction electrons at dynamic and static lattice defects. Solute atoms like S, P, Cr and in particular the ferromagnetic elements Fe, Ni, Co considerably increase the total resistivity. In comparison, the contribution of dislocations is relatively low even at high strains [21]. With increasing content of a second phase or with decreasing dimensions of the constituents the scattering of electrons at phase boundaries substantially degrades the conduction properties of the material.

The fact that the resistivity of pure Cu appears virtually unaffected by deformation (Fig. 6) is not surprising. Since only the cores of the deformation induced dislocations add to the electrical resistivity, but contribute only a very small resistivity change per unit length of a dislocation, the here applied d.c. four-probe technique is not accurate enough for measuring this change. Even for a dislocation density of $10^{16}\,m^{-2}$ the increase of electrical resistivity would amount only $\sim 0.2\,\mu\Omega$mm [21].

The increase of the resistivity of Cu–20%Nb at large strains, $\eta = 6$ (Fig. 6), has to be attributed to the scattering of the conduction electrons at the Cu–Nb phase boundaries. Very high degrees of deformation lead to an extraordinary increase of the amount of internal boundaries because of the curling effect of the Nb filaments. If the filament spacing between two phase boundaries reaches the order of magnitude of the mean free path of a conduction electron, a remarkable drop in conductivity can be expected. According to the present results a filament spacing in the order of 130 nm and a filament thickness of 60 nm can be achieved after the highest attained deformation of $\eta = 10$. Already at $\eta = 7.6$ a filament diameter of about 80–250 nm and a fibre spacing of 150–1000 nm were found. The mean free path of a conduction electron in pure Cu was estimated theoretically [21] and confirmed experimentally [22, 23] as $\ell = 43$–45 nm at 293 K, $\ell = 61$–63 nm at 198 K and $\ell = 138$–145 nm at 77 K. As derived in Appendix 1, for pure Nb, the mean free electron path was theoretically estimated as $\ell = 2$ nm at 293 K, $\ell = 3$ nm at 198 K and $\ell = 10.5$ nm at 77 K. Slightly different values, namely $\ell = 3.1$ nm at 293 K, $\ell = 5$ nm at 198 K and $\ell = 17.6$ nm at 77 K were calculated on the basis of experimental data of Auer and Ullmaier [24]. Since in the theoretical assessment the electron mass and the density of quasi free electrons were merely estimated in accordance to values stemming from related transition metals, the latter data are considered more reliable and will be referred to in the following. On the basis of these data and the current microstructural results the loss of the electrical conductivity with increasing MMC deformation can now be treated more rigorously.

As derived in Appendix 2, for a quantitative assessment of the dependence of resistivity upon fibre geometry in the deformed MMC, the theory of electron scattering at the surface of very thin wires [25, 26] was applied. In the current model, however, the surface is replaced by the phase boundary between Cu and Nb. The two phases thus represent two linear resistors connected parallel, the resistivity of each varies according to its filament thickness. On the basis of this model, the total resistivity ρ depends on ρ_{Cu} and ρ_{Nb} as

$$\frac{1}{\rho} = \frac{0.8}{\rho_{Cu}} + \frac{0.2}{\rho_{Nb}}. \tag{1}$$

As shown in Appendix 2, the dependence of the microstructure upon wire deformation was fitted from experimental data. The obtained results are depicted in Fig. 13 for the three different temperatures investigated. The basic evolution of the resistivity, i.e. especially the experimentally observed increase at large strains is adequately covered by the model. As a result the increase of resistivity in largely strained MMCs can essentially be attributed to scattering of conduction electrons at phase boundaries. However, two deviations from the experimental findings are apparent. First, the calculated resistivities are lower than the experimental ones (Fig. 13). Second, the weak drop of the resistivity which was observed within the range $5 < \eta < 7$, especially at 77 and 198 K, is not covered by the model. The first deviation is attributed to the microstructural data incorporated into the simulation. It was shown by Verhoeven *et al.* [27] that transmission electron

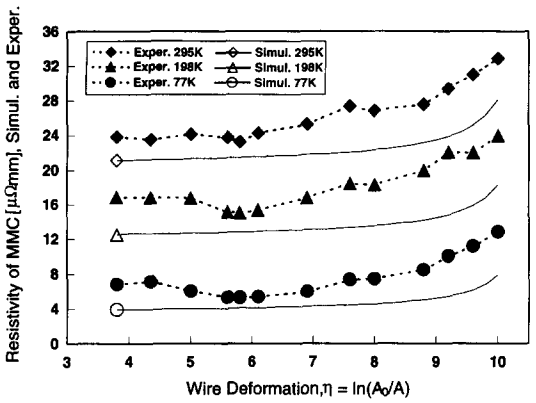

Fig. 13. Resistivity of Cu–20 wt%Nb with progressing wire deformation for three different temperatures. Comparison between experimentally determined and simulated data.

microscopy has to be employed in order to painstakingly record filament diameter and spacing also for heavily deformed Cu–Nb MMCs. It has thus to be considered that the experimentally observed average fibre data are generally too large. If the increase of the resistivity shown in Fig. 6 is entirely attributed to scattering electrons at phase boundaries, a fibre spacing of about 51 nm rather than 130 nm is predicted. Furthermore the real morphology and thus also the amount of the phase boundaries is much more intricate than suggested by the here employed simplified fitting parameters. This shortcoming cannot be easily solved merely by choosing a more adequate description of the internal boundary geometry. Additionally a more appropriate theoretical backbone accounting also for a less simple geometry needs to be developed. As has been analysed previously, the scattering caused by the dislocation content is considered of minor importance. The second deviation, i.e. the resistivity drop within the range $5 < \eta < 7$, is attributed to the initial rotation of the Nb dendrites. As is evident from the microstructural data, up to $\eta = 6$ the dendrites primarily rotate parallel to the drawing axis rather than undergoing large thickness reduction. In this regime the total phase boundary area hence does not increase considerably. However, the scattering cross-sectional fraction imposed by the Nb phase, hindering the current flow in the Cu parallel to the longitudinal direction, is continuously reduced and reaches a minimum when the dendrites are aligned parallel to the drawing axis. In the following, i.e. for $\eta > 6$, the aligned Nb dendrites reveal a massive cross-sectional reduction leading to the observed increase of the resistivity.

The resistivity of the Cu–20%Nb composite changes distinctly on annealing (5 h at 550°C) subsequent to deformation (Fig. 7). At small strains ($\eta < 6$) the general drop of the resistivity ($\leqslant 2\ \mu\Omega$mm) is probably due to the segregation of solute atome to internal boundaries, which serve as sinks. The foreign atoms were presumably of sulphur which might stem from the graphite crucible where they represent the main impurity. Recrystallization of the Cu phase within the MMC is less likely to produce this effect at low strains. The high impurity content of the Cu in the composite is documented by the low value of the residual resistivity ratio which was measured for the pure Cu used to prepare the alloys.

At higher degrees of deformation ($\eta > 6$) the loss of the resistivity during heat treatment of Cu–20%Nb becomes even more evident (Fig. 7). This drop is likely to be due to coarsening of the Nb filaments. For the diffusion controlled coarsening of the ribbons, mass transport can take place along the Cu–Nb phase boundaries, with a much lower energy of activation than for bulk diffusion. According to experimental results [28] and theoretical estimations [29] a coarsening of the Nb filaments must be accounted for at temperatures exceeding 350°C. If one considers the typical two-stage coarsening of filaments which is often observed during annealing of fibre reinforced MMCs [29] the decrease of the total surface area can be assessed. During the first coarsening stage the initially curled Nb filaments form into fibres with a circular cross section to quickly reduce the interface area.

From the data shown in Fig. 7 the coarsening, i.e. the increase of the average fibre spacing can also quantitatively be calculated, provided that the resistivities of the samples prior to annealing are exclusively attributed to scattering at phase boundaries. However, this procedure suggests a fibre spacing which is by average 2.55 times smaller than the data stemming from microscopy. Applying equations (1)–(4) to the observed resistivity drop at $\eta = 10$ (Fig. 7), the average fibre spacing increases from 51 to 122 nm during heat treatment.

The magnetoresistance, i.e. the increase of the resistivity due to an externally imposed magnetic field (Fig. 8) is caused by the Lorenz force which deflects the conduction electrons. Since the magnetic field applied in the current study was perpendicular to the current direction a deflection was caused. The difference of the magnetoresistances of Cu and Cu–20%Nb is a consequence of the different scattering centres for the electrons. Under the influence of an external magnetic field the resistivity of Cu–20%Nb is dominated by the phase boundaries rather than by the Lorentz force. This becomes particularly obvious from Fig. 9, which proves a much higher sensitivity of Cu to a magnetic field than Cu–20%Nb.

With regard to the superconducting properties of the Cu–20%Nb composite, it has first to be emphasized that superconductivity of the complete sample occurred although only 20 wt% of the MMC consist of superconducting Nb, which has a critical temperature of 9.2 K. In the respective microstructure investigation, however, no Nb filaments were observed to have a length comparable to the distance between the voltage leads (12–15 cm). Thus it is not likely that a continuous connection of Nb ribbons existed over the

distance examined. The observed superconductivity hence requires the occurrence of weak links between the isolated Nb filaments. These could be a local penetration of the superconducting state into the Cu matrix (proximity effect) or tunneling of Cooper pairs between the filaments as suggested by Josephson [30]. The observed dependence of the onset of superconductivity on temperature (Fig. 10) and magnetic field (Fig. 11) also suggests the occurrence of weak links rather than superconducting Nb connections between the filaments [30, 31]. With an imposed magnetic field the onset temperature of the less deformed wire is more degraded than that of the heavier deformed specimen (Fig. 10). Moreover the less deformed sample shows a lower critical magnetic field as is evidenced from the corresponding onset temperatures (Fig. 11). Another technologically interesting feature of Cu–20%Nb is the higher stability of the superconducting state compared to pure bulk Nb when exposed to a magnetic field. The upper critical field in pure Nb—extrapolated to $T = 0$ K—is approximately $B = 0.194$ T [32]. Depending on the content of static lattice defects, however, also values up to 1 T have been reported for heavily cold worked Nb [33]. In contrast, in Cu–20%Nb the critical fields of $B = 2$ T or more can be achieved at temperatures below 3 K (Fig. 12) without the loss of superconductivity. Pure Nb is a weak type II superconductor, since the penetration length is within the range of the coherency distance [34]. Internal boundaries of *in situ* formed superconductors, however, are well known to act as effective pinning centres for the magnetic flux lines [34–36]. It is thus strongly suggested that the high critical magnetic field of the type II superconducting Cu–20%Nb is due to the enhancement of internal boundaries. Figure 12 shows the corresponding section of the superconductivity phase diagram of Cu–20%Nb ($\eta = 10$, current density $j = 0.9$ A/mm^2).

5. CONCLUSIONS

The normal and superconducting properties of *in situ* formed Cu–20%Nb composites were investigated and discussed with regard to microstructure evolution and microstructure property correlations. The resistivity of the composite was found to increase with decreasing fibre diameter and filament spacing. This was attributed to the scattering of the conduction electrons at the phase boundaries. The increase of the contribution of scattering at the internal boundaries with decreasing temperature was interpreted by the growing mean free path of the conduction electrons. The magnetoresistance was found to be larger in pure Cu than in Cu–20%Nb. Also weakly deformed Cu–20%Nb samples show a transition into the superconducting state. It was suggested that weak links occur between the Nb filaments and maintain superconductivity. A corresponding microstructural dependence of the superconductivity was found. Cu–20%Nb possibly develops a type II-like superconductivity in which the phase boundaries act as pinning centres for the magnetic flux lines.

Acknowledgements—The authors gratefully acknowledge the kind support by the National High Magnetic Field Laboratory in Tallahassee, Florida, where the measurements of the electromagnetic properties were carried out. A portion of this work was supported by NSF Cooperative Agreement No. DMR-9016241 and by the State of Florida. The authors gratefully acknowledge the kind support by Dr H.-J. Scheider-Muntau, Dr L. T. Summers and Dr E Palm.

REFERENCES

1. D. J. Chakrabati and D. E. Laughlin, *Bull. Alloy Phase Diag.* **2,** 936 (1982).
2. G. I. Terekhov and L. N. Aleksandrova, *Izvest. Akad. Nauk S.S.R. Metally* **4,** 210 (1984).
3. G. Frommeyer, in *Verbundwerkstoffe*, 5. DGM (1981).
4. K. R. Karasek and J. Bevk, *J. appl. Phys.* **52,** 1370 (1981).
5. J. Bevk, J. P. Harbison, J. L. Bell, *J. appl. Phys.* **49,** 6031 (1978).
6. W. A. Spitzig, A. R. Pelton and F. C. Laabs, *Acta metall.* **35,** 2427 (1987).
7. P. D. Funkenbusch and T. H. Courtney, *Acta metall.* **33,** 913 (1985).
8. D. Raabe and U. Hangen, in *Proc. 15th Risø Int. Symp. on Materials Science* (edited by S. I. Andersen, J. B. Bilde-Sorensen, T. Lorentzen, O. B. Pedersen and N. J. Sorensen), p. 487. Risø Nat. Lab., Roskilde (1994).
9. F. Herlach, *I.E.E.E. Trans. Magn.* **24,** 1049 (1988).
10. J. D. Embury, M. A. Hill, W. A. Spitzig and Y. Sakai, *MRS Bull.* **8,** 57 (1993).
11. H.-J. Schneider-Muntau, *I.E.E.E. Trans. Magn.* **18,** 32 (1982).
12. F. Heeringhaus, D. Raabe, L. Kaul and G. Gottstein, *Metall.* **47,** 558 (1993).
13. F. Heringhaus, D. Raabe, U. Hangen and G. Gottstein, Proc. Icotom 10, *Mater. Sci. Forum* **157-162,** 709 (1994).
14. D. Raabe, J. Ball and G. Gottstein, *Scripta metall. mater.* **27,** 211 (1992).
15. A. R. Pelton, F. C. Laabs, W. A. Spitzig and C. C. Cheng, *Ultramicroscopy* **22,** 251 (1987).
16. D. Raabe and G. Gottstein, *J. Phys. IV, col. C7, suppl. J. Phys. III* **3,** 1727 (1993).
17. F. Heringhaus, D. Raabe and G. Gottstein, *Metall.* **48,** 287 (1994).
18. K. R. Karasek and J. Bevk, *J. appl. Phys.* **52,** 1370 (1981).
19. W. F. Hosford Jr, *Trans. TMS A.I.M.E.* **230,** 12 (1964).
20. G. Wassermann, *Verbundwerkstoffe, 63.* DGM (1981).
21. J. G. Rider and C. T. B. Foxon, *Phil. Mag.* **16,** 1133 (1967).
22. F. W. Reynolds and G. R. Stillwell, *Phys. Rev.* **88,** 418 (1952).
23. G. Frommeyer and W. Wassermann, *Physica status solidi (a)* **27,** 99 (1975).
24. J. Auer and H. Ullmaier, *Phys. Rev. B,* **7,** 136 (1973).
25. R. B. Dingle, *Proc. Soc. Lond. Ser.* **201,** 545 (1950).
26. E. H. Sondheimer, *Adv. Phys.* **1,** 1 (1952).
27. J. D. Verhoeven, W. A. Spitzig, F. A. Schmidt, P. D. Krotz and E. D. Gibson, *J. Mater. Sci.* **24,** 1015 (1989).
28. L. S. Chumbley, H. L. Downing, W. A. Spitzig and J. D. Verhoeven, *Mater. Sci. Engng* **A117,** 59 (1989).
29. T. H. Courtney, in *New Development and Applications in Composites* (edited by D. Kuhlmann-Wilsdorf and W. C. Harrigan Jr). TMS-AIME (1978).
30. B. D. Josephson, *Phys. Rev. Lett.* **1,** 251 (1962).

31. W. Buckel, in *Supraleitung*, Vol. 4. Auflage, Weinheim (1990).
32. B. W. Roberts, *J. Chem. Ref. Data* **5,** 581 (1976).
33. U. Hangen and D. Raabe, *Physica status solidi* (a). In press.
34. H. E. Cline, B. P. Strauss, P. M. Rose and J. Wulff, *J. appl. Phys.* **37,** 5 (1966).
35. F. Habbal and J. Bevk, *J. appl. Phys.* **54,** 6543 (1983).
36. D. Raabe and F. Heringhaus, *Physica status solidi (a)* **142,** 473 (1994).
37. Ch. Kittel, *Introduction to Solid State Physics*, 6th edn. Wiley, New York (1986).

APPENDIX 1

Since no reliable experimental data for the mean free electron path in Nb are available from the literature, the following calculation was executed

$$\ell_0 = v_F \tau \tag{1}$$

where ℓ_0 is the mean free path of a conduction electron in Nb, v_F, the the electron velocity at the Fermi border and τ the relaxation time for steady state conditions. The electron velocity, v_F, can be calculated from the Fermi energy, E_F, and the effective electron mass m^*.

$$v_F = \sqrt{\frac{2 \times E_F}{m^*}}. \tag{2}$$

The Fermi energy, E_F, is connected with the Fermi temperature, T_F

$$E_F = k_B \times T_F \tag{3}$$

where k_B is the Boltzman constant. The Fermi temperature can be computed from the contribution of the quasi free electrons to the specific heat, γ, the value of which has been given by various authors, e.g. [37]

$$T_F = \frac{\pi \times N_L \times k_B}{2 \times \gamma} \tag{4}$$

where N_L is the Avogadro constant. If the relaxation time is calculated according to

$$\tau = \frac{m^*}{n \times e^2 \times \rho} \tag{5}$$

where n is the electron concentration, e the elementary charge and ρ the experimentally observed resistivity, the mean free path of the conduction electrons in Niob can be computed according to

$$\ell_0 = \sqrt{\frac{N_L \times m^*}{\gamma}} \times \frac{\pi \times k_B}{n \times e^2 \times \rho} \tag{6}$$

Since no reliable data are accessible, the effective electron mass, m^*, was set equal to the mass of a free electron and the electron concentration, n, was—in accordance to other 4d transition metals—set equal to $5 \times 10^{28}\ \mathrm{m}^{-3}$.

APPENDIX 2

For a quantitative assessment of the dependence of resistivity upon fibre geometry in the deformed MMC, the theory of electron scattering at the surface of very thin wires [25, 26] was applied. In the current model the surface is replaced by the phase boundary between Cu and Nb. The two phases hence represent two linear resistors connected parallel, the resistivity of each varies according to their filament thickness. For simplicity the Nb filament spacing will be identified with the thickness of the Cu filaments. Both data are available from experiments. The resistivity of each phase can then be determined according to [25, 26]

$$\rho(d) = \rho_0 \left(1 + \frac{3}{4}(1-p)\frac{\ell_0}{d}\right) \tag{1}$$

where $\rho(d)$ is the resistivity as a function of the filament thickness, ρ_0 the resistivity for a sample without scattering at the phase boundary, p the scattering factor, ℓ_0 the mean free path of the conduction electron, and d the thickness of the filament. According to investigations on Cu–Nb it was estimated that p is close to 0 [23, 26]. The suggested approach [equation (1)] is usually applied for $d > \ell_0$. This condition holds for both, Cu ($d/\ell_0 \approx 3$) and Nb ($d/\ell_0 \approx 20$) corresponding to the current data for $\eta = 10$ and $T = 293$ K. Assuming $p = 0$ equation (1) is modified into

$$\rho_{Cu}(d_{Cu}, T) = \rho_{Cu_0}(T) \times \left(1 + \frac{3}{4} \times \left(\frac{l_{Cu}(T)}{d_{Cu}}\right)\right) \tag{2a}$$

$$\rho_{Nb}(d_{Nb}, T) = \rho_{Nb_0}(T) \times \left(1 + \frac{3}{4} \times \left(\frac{l_{Nb}(T)}{d_{Nb}}\right)\right). \tag{2b}$$

Here $\rho_{Cu}(d_{Cu}, T)$ and $\rho_{Nb}(d_{Nb}, T)$ are the resistivities of Cu and Nb as a function of fibre diameter and temperature. For the pure and undeformed constituents, Cu and Nb, the following resistivities were measured on bulk samples: $\rho_{Cu0} = 17\ \mu\Omega$mm and $\rho_{Nb0} = 155\ \mu\Omega$mm at 295 K, $\rho_{Cu0} = 10\ \mu\Omega$mm and $\rho_{Nb0} = 95\ \mu\Omega$mm at 198 K as well as $\rho_{Cu0} = 3\ \mu\Omega$mm and $\rho_{Nb0} = 27\ \mu\Omega$mm at 77 K. From the microstructural data the evolution of the filament thickness with increasing wire deformation can be expressed as

$$d_{Cu}(\eta) = d_{Cu}(0) - k_{Cu} \times \ln(\eta) \tag{3a}$$

$$d_{Nb}(\eta) = d_{Nb}(0) - k_{Nb} \times \ln(\eta) \tag{3b}$$

where $d_{Cu}(\eta)$ is the thickness of the Cu and $d_{Nb}(\eta)$ that of the Nb filaments for a wire deformation η. The experimental results can be fitted in the range, $1 \leqslant \eta \leqslant 10$, by $d_{Cu}(0) = 3609.51$ nm, $k_{Cu} = 1504.25$ nm, $d_{Nb}(0) = 1855.50$ nm and $k_{Nb} = 774.98$ nm. From the approach of parallel connected resistors, the total resistivity ρ depends on ρ_{Cu} and ρ_{Nb}

$$\frac{1}{\rho} = \frac{0.8}{\rho_{Cu}} + \frac{0.2}{\rho_{Nb}}. \tag{4}$$